

Faceting diagram for Ag segregation induced nanofaceting at an asymmetric Cu tilt grain boundary

Nicolas J. Peter^{a,*}, Maria J. Duarte^a, Christoph Kirchlechner^a, Christian H. Liebscher^{a,*},
Gerhard Dehm^a

^a *Max-Planck-Institut für Eisenforschung GmbH, Max-Planck-Strasse 1, 40237 Düsseldorf, Germany*

Abstract

In this work, we experimentally establish the isothermal nanofacet evolution at an asymmetric tilt grain boundary in the Cu-Ag system using a diffusion couple approach. We investigate the nanofacet formation along the grain boundary in dependence of the Ag solute excess concentration. The initial grain boundary dissociates into asymmetric Ag-lean segments and Ag-rich symmetric (210) segments. Increasing Ag excess leads to an increase in Ag-rich facet segment length, while the length of the asymmetric facets remains constant. From this, we construct a grain boundary nanofaceting diagram deduced from our experiments relating local atomic structure, overall inclination and Ag solute excess.

Keywords: Scanning/transmission electron microscopy (STEM), Copper, Copper alloys, Grain boundary segregation

Grain boundaries (GBs) are interfaces separating adjoining crystals with different misorientation. They are amongst the most important material defects and their associated structure and properties determine their influence on the behavior of polycrystalline materials. In early work, Gibbs established that interfacial transitions can be described by equilibrium thermodynamics [1] and Hart later proposed that transitions at GBs are possible and referred to them as “two-dimensional phase transitions” [2]. The thermodynamic description of these transitions was extended by Cahn and Rottman [3, 4] who categorized them into faceting and congruent (all 5 degrees of freedom remain constant) transitions. Both types, non-congruent (faceting) and congruent transitions are referred to as GB phase transformations [5] or synonymously GB complexion transitions [6, 7]. However, these transitions are typically studied in perfectly symmetric and planar GBs [8–10] and mostly derived from indirect experimental measurements [11, 12] or atomistic simulations [13]. Instances of how complex such GB transitions can be and how factors like temperature and chemistry can influence a GB’s structure were recently demonstrated by scanning transmission electron microscopy (STEM). Hu et al. found a temperature dependent segregation behavior

*Corresponding author.

Email addresses: peter@mpie.de (Nicolas J. Peter), duarte@mpie.de (Maria J. Duarte), kirchlechner@mpie.de (Christoph Kirchlechner), liebscher@mpie.de (Christian H. Liebscher), dehm@mpie.de (Gerhard Dehm)

including a first order congruent transition at low temperatures in a planar Au-doped Si GB using atomistic calculations [14]. Very recently, a complex co-segregation pattern including segregation induced symmetry changes and order losses at a planar WC grain boundary was discovered [15]. A comprehensive review on evidence of grain boundary transitions can be found in a recent review article [16].

Already Cahn discussed that most GB transitions involve faceting [3] and such transitions have been observed experimentally in many materials [17–19]. Faceting-roughening phenomena of GBs were recently summarized by Straumal et al. for a great amount of different grain boundary types and in different material systems [20]. The majority of experimental and simulation work established a clear dependence of faceting-defaceting transitions on temperature in pure metal GBs [18, 21–23]. Some work also focused on how structural defects of a grain boundary (GB dislocations) may influence faceting by pinning or dragging facets during defect motion [24]. Transitions influenced by chemical stimulus, for instance by segregation, are much less understood in the case of GB faceting as compared to the segregation behavior of planar boundaries. Changing the chemistry at GBs by adsorption of solute excess significantly changes the energy of such boundaries and consequently structural transitions are likely to occur. Early work showed structural transitions at a low angle grain boundary in the Fe-Au system [25]. Faceting transitions were frequently observed in the last decades in the Cu-Bi binary system since Bi promotes GB embrittlement [26]. Experimentally, only one carefully performed *in situ* experiment conducted by Ferenc and Baluffi unambiguously demonstrated that reversible faceting-defaceting can be induced by solute adsorption [27]. However, faceting occurred on a scale of several tens to hundreds of nanometers and the characterization of the atomic GB structure and chemistry was not possible at that time. Four decades ago Loier and Boos demonstrated already how small additions of Bi induce striations and faceting of Ni grain boundaries [28]. Yu et al. recently found distinct segregation patterns of Bi solutes at a microfaceted general GB in Ni [29] after having shown that such patterns may be the underlying reason for detrimental effects of Bi segregation on mechanical properties in Ni [30]. Our recent work combining atomic resolution imaging and atomistic modelling demonstrated that Ag segregation can act as chemical trigger promoting a nanofaceting transition of an asymmetric tilt grain boundary in Cu [31]. However, temperature [32], pressure [33] or solute excess concentration [27, 34] strongly influence GB transitions [35] and their concentration dependence is usually established by atomistic modeling.

Here, we report the experimental assessment of GB plane and faceting evolution in dependence on the Ag solute excess concentration at an initially asymmetric tilt grain boundary in Cu. The concentration dependence was observed using atomic resolution STEM in combination with energy dispersive X-ray spectroscopy (EDS) and atom probe tomography (APT) in close vicinity to the interface of a Cu-Ag diffusion couple. A Ag reservoir was sputter deposited on top of a bicrystal containing the GB to create the diffusion couple. For consistency, we refer to the surface of the bicrystal (the interface to the Ag reservoir) as surface.

A pure Cu reference boundary of the bicrystal’s top surface before Ag deposition was observed at three distinct magnifications (Fig. 1b). Temperature induced faceting of that

boundary was already excluded in our previous work [31]. The boundary appears to be entirely flat for at least 13 μm from the top surface into the bulk as determined by STEM, even at higher magnification. Atomic resolution imaging reveals the local atomic arrangement and although some sub-nanometer roughness can be associated to the asymmetric GB; we refer to this boundary as flat reference boundary. The reference GB was determined to be close to an asymmetric $34^\circ[001] (920)/(110)$ boundary, which is in close agreement to our previously investigated GB showing the Ag induced nanofaceting [31]. After Ag diffusion, the overall macroscopic grain boundary (observed at low magnification) is no longer straight and a seemingly continuous curvature from the bulk to the surface was induced. A schematic representation of the grain boundary after segregation is given in Fig. 1a) and an experimental HAADF STEM micrograph of a part of the grain boundary close to the surface at low magnification in Fig. 2. Micrographs were then acquired at certain locations and at high magnifications along the segregated GB to study the overall plane evolution connected with the nanofacet formation and the associated Ag excess. Representative locations (see Fig. 2 positions 4 to 1, from Cu(Ag) GB close to the surface) are marked in the overview image and are presented in more detail below. We observe a gradual transition from a flat segregated boundary (1 in Fig. 2, compare STEM-EDS results), in close resemblance to the Ag-free reference, to a symmetric $\sum 5 (210)$ GB (4 in Fig. 2) as further indicated by the adoption of the kite motif [13, 31] in the enlarged area next to the micrograph of position 4. The intermediate GB adopts a nanofaceted state containing Ag-rich, symmetric $\sum 5 (210)$ segments and newly formed, asymmetric and Ag-lean segments with a GB plane close to $(320)/(100)$. Almost all kite tip positions are occupied by Ag (bright columns in HAADF STEM). In addition, we occasionally observe image contrast indicating Ag occupation of non-kite tip positions at the GB, as well. Therefore it is reasonable to believe that the symmetric GB close to the surface is covered close to a monolayer of Ag. The symmetric $\sum 5 (210)$ GB plane was measured to be $\sim 20^\circ$ inclined with respect to the non-faceted, asymmetric $(920)/(110)$ reference boundary plane.

The precise solute excess concentration and localized elemental distribution were determined along the boundary by APT and STEM-EDS, respectively. An APT specimen extracted close to the sample surface (Tip 1, position 4 in Fig. 2) was found to have a peak concentration of ~ 3.6 at. % Ag (black line) as determined from the integrated line profiles across the GB (Fig. 3a, upper graph). A specimen extracted from below the sample surface (Tip 2, at position 3 in Fig. 2) only contained a peak solute excess of ~ 2.4 at. % Ag (Fig. 3a, lower graph). A depletion zone is visible for the Ag concentration next to the enriched GB in both specimen. In the case of the less segregated GB (Tip 2), the Ag concentration recovers towards the outer APT needle's surface and reaches saturation at a level of about 1.3 at. % at about 25 nm from the GB. For Tip 1, the depletion extends much further and saturation is not reached inside the specimen volume. From the course of the concentration profile we expect a saturation level of around 1.7 at. % at about 45 nm from the GB deduced from a second order polynomial fitting. To determine the respective bulk Ag concentration more reliable, we created cylinders of the same dimensions (25 nm x 10 nm x 40 nm) inside the two volumes and placed them parallel to the GB at a fixed distance of 20 nm (in saturation level of Tip 2). Bulk concentrations of 1.43 ± 0.015 at.

% and 1.23 ± 0.011 at. % were extracted for Tip 1 and Tip 2, respectively. The precise location of the extracted tips within a few μm is hardly possible to be determined after FIB milling preparation. The bulk Ag concentrations appear reasonable considering the low Ag solubility according to the equilibrium phase diagram [36]. In addition, Ag density maps of thin slices (1 nm thickness) through the reconstructed volumes of these two APT tips - one from a surface-near region (Tip 1) and one extracted from an approximate location 3 in Fig. 2 (Tip 2) - revealed a non-faceted, Ag-rich boundary close to the surface and further towards the bulk a faceted, Ag-rich boundary. This transition agrees well with our experimental STEM micrographs. Across these two boundaries we calculated the solute excess concentration following our previously applied approach [31, 37] and revealed for Tip 1 a Ag excess concentration of $4.96 \text{ at}/\text{nm}^2$, while the faceted GB (Tip 2) showed an average excess concentration of $3.39 \text{ at}/\text{nm}^2$. Based on the latter, we chose a maximum value for the color bar to qualitatively best show the faceted GB state. These results appear reasonable, as STEM results revealed preferential segregation to symmetric $\Sigma 5$ (210) GB portions, which dominate at the surface, but contribute less for deeper measurement locations into the bulk due to the increasing incorporation of asymmetric Ag-lean segments. In addition, the diffusion gradient from the surface into the bulk reduces the Ag excess concentration at the GB, which therefore appears to be coupled with the facet lengths. The excess of the non-faceted, symmetric $\Sigma 5$ (210) boundary close to the surface is just slightly below the monolayer solute excess of roughly $6 \text{ at}/\text{nm}^2$, which is calculated by the number of atoms on a (210) plane unit area. However, STEM micrographs at the very surface revealed some areas in which two bright atomic columns appear next to each other, which is why we assume to have at least monolayer coverage at the very surface of the diffusion couple, i.e. close to the Ag reservoir. The drawback of such compositionally sensitive APT measurements is the lack of atomically resolved structural features in the analyzed volume. Consequently, STEM-EDS was used in order to correlate the occurrence of the three structural states observed with their solute excess at different locations along the segregated boundary. Integrated intensity line profiles for the Ag- L_α peak were extracted from EDS maps at the investigated locations and three representative profiles (close to positions 1, 2 and 4) for the three observed GB states are plotted after applying of a moving average algorithm for visibility in Fig. 3b) normalized to the background intensity. The inset shows EDS spectra integrated in a region of about $10 \times 15 \text{ nm}^2$ of the expected Ag- L_α peak for a GB containing area and an area inside one grain for comparison. We would like to point out that EDS maps were acquired in zone axis orientation immediately after image acquisition to avoid tilting and loss of spatial correlation. In this case, quantification of the EDS data is no longer applicable through the Cliff-Lorimer method and intensive simulation work would have to be performed to account for effects like beam spreading and electron channelling [38]. Therefore, we do not give absolute concentration values from EDS but normalize our results to the concentration expected for monolayer coverage by integrating the peak intensity and collapsing it to a GB width of 0.12 nm, as this width provides a Ag reference concentration of 100 % for the data set closest to the surface. This assumption is based on our experimental HAADF STEM results. STEM-EDS analyses show a clear increase of Ag from the bulk towards the surface.

The combination of structural and compositional characterization of the observed faceting evolution enables a comprehensive view on the evolution of individual facet segments. In fact, we composed a segregation-induced GB faceting diagram for the investigated GB under the chosen diffusion conditions (Fig. 4). Plotting the facet segment length against the relative Ag monolayer coverage (Fig. 4a) as determined by EDS along the GB (Fig. 3b) reveals a concentration window for faceting to occur. While the asymmetric facet segment length was found to be independent of the Ag excess and remained at a length l of about 1 nm, the symmetric facet segments almost linearly grew with increasing excess concentration starting from 1 nm (R-square of 0.96). Therefore, the reason for an increasing global GB inclination lies in growing symmetric facet segments. Thus there are three clearly distinguishable GB states as a function of overall Ag excess solute: (i) non-faceted, asymmetric and Ag-lean (Figure 2-1), (ii) preferentially Ag segregated and nanofaceted (Figure 2-2 and 2-3) as well as (iii) non-faceted, symmetric and Ag-rich (Figure 2-4).

The present results confirm our previous findings [31] that after Ag segregation induced facet formation there is preferential segregation occurring to only the symmetric facet segments, while the asymmetric segments remain Ag-lean. To make a better connection between facet segment length, Ag segregation and especially overall GB inclination, we plotted the relative Ag excess concentration as obtained by EDS under the assumption of full monolayer coverage for the symmetric $\sum 5$ (210) GB close to the surface (Fig. 4b). At this point, the boundary was about 20° inclined from the asymmetric reference GB. To describe the relation between Ag concentration and facet length, we normalize the ratio of the asymmetric segment length (ASL) and the symmetric facet segment length (SSL) using the “facet segment ratio” parameter FSR. FSR is calculated as $FSR = SSL / (ASL + SSL)$. Consequently, the Ag-rich, symmetric $\sum 5$ (210) GB close to the surface does not show any faceting and $FSR = 1$ ($ASL = 0$). The purely asymmetric reference GB at inclination 0° has consequently no symmetric segments and thus $FSR = 0$. The ASL was determined above to be approximately constant with a length of ~ 1 nm for the faceted GB. Under the assumption of full monolayer coverage for $FSR = 1$ supported by STEM observations, we drew a dashed line (red) to indicate an anticipated linear decrease of Ag excess with a linearly decreasing amount of the symmetric segment fraction. Our experimental results are given as individual data points and are linearly fitted (white) with a R-square value of 0.93. Indeed, our results follow the anticipated, ideal line in reasonable agreement (compare red and white lines), which leads us to the conclusion that for the nanofaceted boundary portion symmetric facet segments always are at least close to monolayer coverage, while it indicates that asymmetric segments of the nanofaceted grain boundary section are close to being Ag-free. This extends our previous findings deduced from a GB faceted at a single Ag concentration to the entire faceting range. No faceting was observed below $FSR = 0.5$, which means below these equisized nanofacets, faceting disappears and a purely asymmetric GB takes up the Ag excess. However, the excess uptake does not exceed about 30 % of the symmetric $\sum 5$ (210) GB’s excess. This does not necessarily imply a generally fixed saturation level, as it depends on the local chemical potential, which is influenced also by the annealing temperature and subsequent cooling/quenching conditions. In light of an extrapolation of the facet data to $FSR = 0$ in Figure 4b (white dashed line), the asymmetric GB should have a Ag

concentration of around 16 % of a $\sum 5$ (210) boundary. As this is less than the actually observed 30 %, the asymmetric GB seems much more favorable to be preserved compared to inducing a GB dissociation. This agrees well with our previous MD simulation results, which indicate Ag solute excess being absorbed at the asymmetric boundary already starting at a chemical potential around $\mu = 0.35 \text{ eV}$, while the symmetric $\sum 5$ (210) boundary starts taking up Ag only above chemical potentials of $\mu = 0.5 \text{ eV}$ [31]. Thus, Ag uptake of the asymmetric boundary before the threshold concentration seems to be a prerequisite to induce the nanofaceting. Finally, the jump from about 30 % relative Ag monolayer coverage (FSR = 0) to about 50 % when nanofaceting is induced, strongly indicates a first order GB transition occurring.

Our experimental findings enable us to propose a mechanistic picture of the observed faceting phenomenon. We showed previously experimentally and by simulations that heat treatment at 800°C (1073 K) does not induce nanofaceting at the asymmetric GB studied here, while Ag segregation does. Consequently, heating the boundary to 800°C leaves the boundary intact, possibly with increased disorder. Mishin and co-workers showed in a series of studies on Cu-Ag GBs that increasing temperature, but also increasing Ag solute excess can significantly influence how ordered a GB is referred to the perfect bulk lattice [39–42]. At such high temperatures, Ag atoms are going almost completely in solid solution and diffuse from the surface through the bulk and along the boundary creating a Ag concentration gradient. The solidus line was likely not crossed, as no homogeneous nucleation of Ag precipitates was observed inside the grains. Upon cooling, the disordered grain boundary restores its low temperature structure, while still remaining in the solid solubility region according to the equilibrium phase diagram [36]. Judging from the determined bulk Ag concentration of about 1.5 at. %, the solidus line is crossed at around 550°C (823 K). At this point, Ag starts to segregate towards the GB upon further cooling to minimize the energy of the system. The amount of Ag segregating to the boundary is depth dependent due to the created concentration gradient. Eventually, a critical threshold concentration is reached to initiate nucleation of the symmetric $\sum 5$ (210) facets, since the observed normal kite structure (Fig. 2, 2-4) can absorb the highest amount of Ag excess and leads to the largest reduction in energy compared to segregation to the initial asymmetric GB [31]. The nucleation of symmetric Ag-rich facets is the initial step dissociating the asymmetric GB into a nanofaceted boundary. The local amount of Ag solute excess at the boundary, which is dictated by the concentration gradient in the bulk, determines the density of nucleation sites and provides the driving force for facet growth. Following the trend of having more Ag towards the surface, symmetric facets grow longer towards the surface until a continuous $\sum 5$ (210) GB is formed close to the surface. Below an estimated critical Ag threshold concentration of around 0.6 at.% for the bulk Ag content faceting will not occur considering a constant segregation factor ($\beta = \frac{GBconcentration}{Bulkconcentration}$). However, as the bulk diffusion gradient cannot be quantified here accurately, the threshold concentration cannot be determined precisely neither. The nucleation of the Ag-rich $\sum 5$ (210) facet segments at the initially asymmetric GB is accompanied by the nucleation of the asymmetric facet segment and the associated GB disconnections or facet junctions, which are also necessary to migrate the boundary to compensate for the overall change in inclination towards the surface. The

defects are likely involved in the migration of the GB to compensate for the inclination change induced by nucleation the symmetric facet segments. For instance, the migration of a flat, symmetric GB was shown theoretically for an Al $\Sigma 7$ GB to function via a nucleation process of islands on the grain boundary plane [43] (also regarded as disconnection nucleation for $\Sigma 13$ and $\Sigma 17$ Cu boundaries [44, 45]) and to be highly temperature dependent between 500 K to 700 K [43], which is close or even in the temperature range we expect our facet nucleation to occur. The question remains, why a nanofaceted GB portion is found instead of coarse facets or even just a curved GB. In general, the energy of faceted GB following Hamilton et al. is composed of two parts: (i) the contribution of the GB energies of the two facet segments $\gamma_{1,2}$ along with the contribution of facet junctions γ_j as well as (ii) the interaction between facet junctions γ_{j-j} . The overall GB energy γ_{GB} can thus be described as $\gamma_{GB} = \gamma_1 + \gamma_2 + \frac{2\gamma_j}{\Lambda} + \frac{\gamma_{j-j}}{\Lambda}$, with Λ being the facet period (length). For our purposes we neglect the interaction of the junction term here leading to $\gamma_{GB} = \gamma_1 + \gamma_2 + \frac{2\gamma_j}{\Lambda}$. Hamilton et al. demonstrated by simulation work that the GB inherently wants to create equal sized, coarse facets to reduce the spacing of the GB facet junctions and thus γ_{GB} as much as possible [46]. Although this theory was confirmed experimentally by Medlin et al. [47] and atomistic simulations by Wu et al. [48], this analysis does not consider segregation and kinetic effects. Wu et al. found that migration kinetics during facet coarsening can promote the formation of finite sized facets. Instead of a continuous decrease in energy for increasing facet periods, migration of facet segments can impose a multitude of energy barriers depending on the structure of the facet segment resulting in the inhibition of further migration and therefore stabilization of finite length facets. Here, the energy change due to segregation can be expressed generally through $\Delta\gamma_{GB} = \Delta\gamma_{ASL} + \Delta\gamma_{SSL} + \frac{2\Delta\gamma_j}{\Lambda}$. However, considering the preferential segregation only to the symmetric portion and no noticeable segregation to facet segment junctions, the energy reduction is mainly attributed to the reduction in energy due to the formation of symmetric $\Sigma 5$ (210) segments thus following $\Delta\gamma_{GB} = \Delta\gamma_2$. Nevertheless, it would be interesting to study effects of segregation to junctions and how they influence the energetics of the systems including the interaction between junctions, which was neglected here. Segregation to facet junctions was for example recently observed at faceted Si [49] and Cu GBs [50].

In conclusion, we present the first GB faceting diagram by studying the influence of Ag solute excess concentration on facet formation in an asymmetric tilt grain boundary via aberration corrected STEM, STEM-EDS and APT. After having established a Ag concentration gradient by a diffusion couple approach, we were able to distinguish different structural arrangements (faceting states) along the boundary as a function of Ag solute excess concentration. The total length of the $\Sigma 5$ GB increases by more than 15% compared to its initial (Ag-free) position, revealing a lower energy state after Ag segregation. In the bulk at low Ag solute excess relative to the surface, the initially asymmetric GB remains structurally unaffected but takes up Ag. Exceeding a threshold amount of solute excess, the boundary undergoes a first order transition and becomes nanofaceted. One facet segment changes its grain boundary plane, but remains asymmetric, Ag-lean and constant in length, while the other segment was determined to be a symmetric $\Sigma 5$ (210) type, with increasing

length towards the surface and being enriched in Ag. At the surface, highest amounts of available Ag allow for a planar $\Sigma 5$ (210) GB containing close to a monolayer of Ag. Similar GB phase diagrams have been established for different transitions like GB premelting, intergranular film formation or for multilayer segregation patterns as a function of concentration [16]. However, only few such GB phase diagrams could be established, yet. We present here the first experimental GB nanofaceting diagram as a function of solute excess concentration, similar to GB segregation diagrams as proposed by Lejček and Hofman for iron GBs [51] or Watanabe et al.'s hardening/segregation GB diagrams in iron alloys [52], but focusing on the atomic grain boundary structure evolution. Establishing such diagrams, analogous to bulk phase diagrams, may offer new possibilities for microstructure engineering in order to tune macroscopic materials properties. Although the preferential segregation might appear as an exception from the Langmuir McLean adsorption behavior in terms of homogeneous GB decoration, the individual segments still follow Langmuir McLean. Regarding the asymmetric segregated and the symmetric $\Sigma 5$ (210) GB, we were able to use the Langmuir McLean relation to deduce the ratio of their respective segregation energies and found that the Gibbs segregation energy of the symmetric boundary is approximately 1.08 times the energy of the asymmetric GB. Nevertheless, adjusted segregation models accounting for such faceting transitions are becoming necessary for these cases. It has to be noted that a continuously curved grain boundary, in contrast to a faceted boundary may be connected differently to physical properties such as mobility or plastic deformation. In fact, continuous curvatures at lower magnifications might be related to nanofaceting transitions as observed in the present study more often for doped material systems. Still, such phenomena would only be resolved with adequate characterization techniques of highest resolution.

Methods

Bicrystal growth and sample preparation. To achieve the structure-chemistry correlation for Ag segregation induced nanofaceting, we grew a Cu bicrystal containing the asymmetric grain boundary using the Bridgman technique. The [001] crystallographic directions of the two seed crystals were aligned parallel with a misorientation of 54° around this common axis to ensure the formation of a tilt GB with a common [001] zone axis orientation, important for the STEM analysis. Additionally, an asymmetric inclination of 31° was chosen for the as-grown reference boundary. From the grown bicrystal, discs were cut perpendicular to the [001] growth direction and metallographically prepared to obtain best surface quality with a final electropolishing step. A reference lamella was extracted from this disc for STEM investigations using focused ion beam (FIB) preparation. Segregation was achieved by thermal annealing at 800°C under high vacuum conditions for 120 hours. In our previous work we could exclude already that these conditions influence the pure, Ag-free, grain boundary structure [31]. Ag was sputter deposited to a thickness of 500 nm onto the same disc used as reference, to extract a Ag segregated GB as close to the reference state as possible. In this way a diffusion couple arrangement was created between Ag and the GB-containing Cu. No additional metallographic preparation was performed to not alter the state of the GB artificially. Thus, although a slight spatial misalignment, we believe to

examine the same GB before and after the diffusion process.

Scanning transmission electron microscopy. The FIB prepared lamella was investigated after thermal treatment using a probe-corrected STEM in a Thermo Fischer Scientific Titan Themis 60-300 STEM machine. A schematic overview of the crystallography and diffusion couple geometry is provided in Fig. 1(a). The shown micrographs were acquired in high-angle annular dark field imaging conditions to benefit from its Z-contrast conditions, i.e. the semi-collection angle was set to 76 - 200 mrad. EDS maps were acquired at selected locations to correlate nanofaceting with Ag solute excess concentration in zone axis orientation immediately after image acquisition to avoid tilting and thus loss of spatial correlation. A Super-X windowless EDS detector was used at an acceleration voltage of 300 kV.

Atom probe tomography. Quantification of Ag excess concentration at the GB with respect to the matrix was obtained from atom probe tomography (APT) reconstructions at specific regions of interest. APT tips were prepared by FIB (same instrument used for TEM lamellae) [53], applying a final cleaning at 5 kV and 41 pA, ensuring a Ga content <0.1 at.% in the analyzed regions. APT data was collected using a local electrode atom probe, LEAP 5000XS by Cameca Instruments. The measurements were performed at a temperature of 50 K, in laser mode with an energy of 60 pJ, using a pulse repetition rate of 250 kHz and a detection rate of 0.007 atoms per pulse.

Acknowledgments

The authors cordially thank Tobias Oellers from the Ruhr University Bochum for Ag deposition on our Cu bicrystals to create the investigated diffusion couples. The funding and support by the European Research Council (ERC) under the EU's Horizon 2020 Research and Innovation Programme is gratefully acknowledged by NJP, MJD and GD (ERC Advanced Grant, GB-Correlate, Grant No. 787446).

References

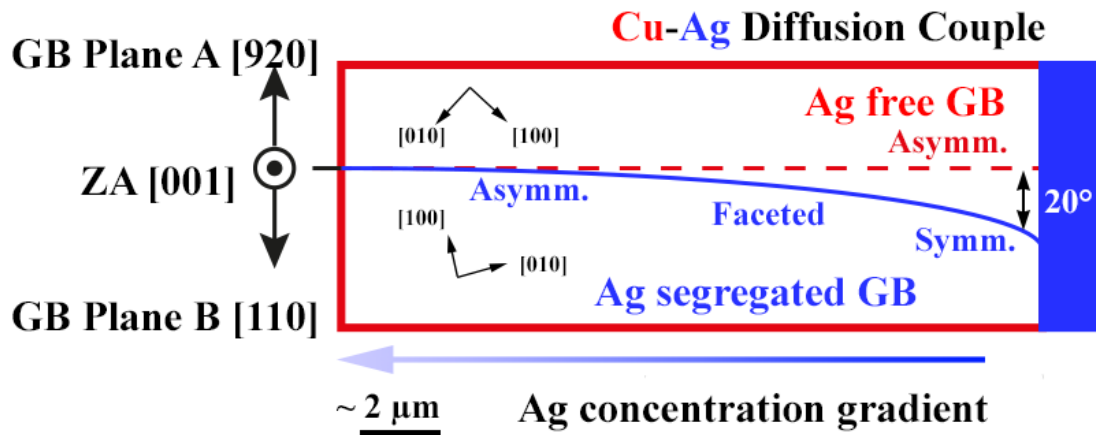
References

- [1] Gibbs, J. W. *The Collected Works of J. Willard Gibbs-Volume 1: Thermodynamics* (Yale University Press, 1945).
- [2] Hart, E. W. Two-dimensional phase transformation in grain boundaries. *Scripta Metall.* **2**, 179–182 (1968).
- [3] Cahn, J. Transitions and phase equilibria among grain boundary structures. *J. Phys. Colloq.* **43**, C6–199 (1982).
- [4] Rottman, C. Theory of phase transitions at internal interfaces. *Le Journal de Physique Colloques* **49**, C5–313 (1988).
- [5] O'Brien, C., Barr, C., Price, P., Hattar, K. & Foiles, S. Grain boundary phase transformations in ptau and relevance to thermal stabilization of bulk nanocrystalline metals. *J. Mater. Sci.* **53**, 2911–2927 (2018).
- [6] Dillon, S. J., Tang, M., Carter, W. C. & Harmer, M. P. Complexion: A new concept for kinetic engineering in materials science. *Acta Mater.* **55**, 6208–6218 (2007).
- [7] Kaplan, W. D., Chatain, D., Wynblatt, P. & Carter, W. C. A review of wetting versus adsorption, complexions, and related phenomena: the rosetta stone of wetting. *Journal of Materials Science* **48**, 5681–5717 (2013).

- [8] Duscher, G., Chisholm, M. F., Alber, U. & Rühle, M. Bismuth-induced embrittlement of copper grain boundaries. *Nature materials* **3**, 621–626 (2004).
- [9] Meiners, T., Frolov, T., Rudd, R. E., Dehm, G. & Liebscher, C. H. Observations of grain-boundary phase transformations in an elemental metal. *Nature* **579**, 375–378 (2020).
- [10] Parajuli, P. *et al.* Misorientation dependence grain boundary complexions in $\langle 111 \rangle$ symmetric tilt al grain boundaries. *Acta Materialia* **181**, 216–227 (2019).
- [11] Divinski, S. V., Edelhoff, H. & Prokofjev, S. Diffusion and segregation of silver in copper σ 5 (310) grain boundary. *Phys. Rev. B* **85**, 144104 (2012).
- [12] Prokoshkina, D., Esin, V. A. & Divinski, S. V. Experimental evidence for anomalous grain boundary diffusion of Fe in Cu and Cu-Fe alloys. *Acta Materialia* **133**, 240–246 (2017).
- [13] Frolov, T., Divinski, S. V., Asta, M. & Mishin, Y. Effect of interface phase transformations on diffusion and segregation in high-angle grain boundaries. *Phys. Rev. Lett.* **110**, 255502 (2013).
- [14] Hu, C. & Luo, J. First-order grain boundary transformations in Au-doped Si: Hybrid Monte Carlo and molecular dynamics simulations verified by first-principles calculations. *Scripta Materialia* **158**, 11–15 (2019).
- [15] Luo, Z. *et al.* A highly asymmetric interfacial superstructure in WC: Expanding the classic grain boundary segregation and new complexion theories. *Materials Horizons* **7**, 173–180 (2020).
- [16] Cantwell, P. R. *et al.* Grain boundary complexion transitions. *Annual Review of Materials Research* **50**, 465–492 (2020).
- [17] Donald, A. & Brown, L. Grain boundary faceting in Cu-Bi alloys. *Acta Metallurgica* **27**, 59–66 (1979).
- [18] Choi, J. S. & Yoon, D. Y. The temperature dependence of abnormal grain growth and grain boundary faceting in 316L stainless steel. *ISIJ Int* **41**, 478–483 (2001).
- [19] Koo, J. B. & Yoon, D. Y. The dependence of normal and abnormal grain growth in silver on annealing temperature and atmosphere. *Metallurgical and Materials Transactions A* **32**, 469–475 (2001). URL <https://doi.org/10.1007/s11661-001-0063-4>.
- [20] Straumal, B., Kogtenkova, O., Gornakova, A., Sursaeva, V. & Baretzky, B. grain boundary faceting–roughening phenomena. *Journal of materials science* **51**, 382–404 (2016).
- [21] Barg, A., Rabkin, E. & Gust, W. Faceting transformation and energy of a σ 3 grain boundary in silver. *Acta Metall. Mater.* **43**, 4067–4074 (1995).
- [22] Bowers, M. L., Ophus, C., Gautam, A., Lancon, F. & Dahmen, U. Step coalescence by collective motion at an incommensurate grain boundary. *Phys. Rev. Lett.* **116**, 106102 (2016).
- [23] Brown, J. A. & Mishin, Y. Dissociation and faceting of asymmetrical tilt grain boundaries: Molecular dynamics simulations of copper. *Phys. Rev. B* **76**, 134118 (2007).
- [24] Shibata, N., Oba, F., Yamamoto, T., Sakuma, T. & Ikuhara, Y. Grain-boundary faceting at a = $3[110]/\{112\}$ grain boundary in a cubic zirconia bicrystal. *Philosophical Magazine* **83**, 2221–2246 (2003).
- [25] Sickafus, K. E. & Sass, S. Grain boundary structural transformations induced by solute segregation. *Acta Metallurgica* **35**, 69–79 (1987).
- [26] Sigle, W., Ciiang, L.-S. & Gusr, W. On the correlation between grain-boundary segregation, faceting and embrittlement in Bi-doped Cu. *Philos. Mag. A* **82**, 1595–1608 (2002).
- [27] Ference, T. & Balluffi, R. Observation of a reversible grain boundary faceting transition induced by changes of composition. *Scripta Metall.* **22**, 1929–1934 (1988).
- [28] Loier, C. & Boos, J. Striation and faceting of grain boundaries in nickel due to sulfur and other elements. *Metallurgical Transactions A* **12**, 129–135 (1981).
- [29] Yu, Z. *et al.* Segregation-induced ordered superstructures at general grain boundaries in a nickel-bismuth alloy. *Science* **358**, 97–101 (2017).
- [30] Luo, J., Cheng, H., Asl, K. M., Kiely, C. J. & Harmer, M. P. The role of a bilayer interfacial phase on liquid metal embrittlement. *Science* **333**, 1730–1733 (2011).
- [31] Peter, N. J. *et al.* Segregation-induced nanofaceting transition at an asymmetric tilt grain boundary in copper. *Physical review letters* **121**, 255502 (2018).
- [32] Frolov, T., Olmsted, D. L., Asta, M. & Mishin, Y. Structural phase transformations in metallic grain

- boundaries. *Nature communications* **4**, 1–7 (2013).
- [33] Harris, D. J., Watson, G. W. & Parker, S. C. Computer simulation of pressure-induced structural transitions in mgo [001] tilt grain boundaries. *American Mineralogist* **84**, 138–143 (1999).
 - [34] Frolov, T., Asta, M. & Mishin, Y. Segregation-induced phase transformations in grain boundaries. *Physical Review B* **92**, 020103 (2015).
 - [35] Frolov, T. & Mishin, Y. Thermodynamics of coherent interfaces under mechanical stresses. ii. application to atomistic simulation of grain boundaries. *Physical Review B* **85**, 224107 (2012).
 - [36] Subramanian, P. & Perepezko, J. The ag-cu (silver-copper) system. *J. Phase Equilib.* **14**, 62–75 (1993).
 - [37] Felfer, P. J. *et al.* A quantitative atom probe study of the nb excess at prior austenite grain boundaries in a nb microalloyed strip-cast steel. *Acta Materialia* **60**, 5049–5055 (2012).
 - [38] Kothleitner, G. *et al.* Quantitative elemental mapping at atomic resolution using x-ray spectroscopy. *Physical Review Letters* **112**, 085501 (2014).
 - [39] Williams, P. & Mishin, Y. Thermodynamics of grain boundary premelting in alloys. ii. atomistic simulation. *Acta Materialia* **57**, 3786–3794 (2009).
 - [40] Suzuki, A. & Mishin, Y. Atomic mechanisms of grain boundary diffusion: Low versus high temperatures. *Journal of materials science* **40**, 3155–3161 (2005).
 - [41] Koju, R. & Mishin, Y. Relationship between grain boundary segregation and grain boundary diffusion in cu-ag alloys. *arXiv preprint arXiv:2006.06591* (2020).
 - [42] Hickman, J. & Mishin, Y. Disjoining potential and grain boundary premelting in binary alloys. *Physical Review B* **93**, 224108 (2016).
 - [43] Hadian, R., Grabowski, B., Race, C. P. & Neugebauer, J. Atomistic migration mechanisms of atomically flat, stepped, and kinked grain boundaries. *Physical Review B* **94**, 165413 (2016).
 - [44] Combe, N., Momprou, F. & Legros, M. Disconnections kinks and competing modes in shear-coupled grain boundary migration. *Physical Review B* **93**, 024109 (2016).
 - [45] Rajabzadeh, A., Momprou, F., Legros, M. & Combe, N. Elementary mechanisms of shear-coupled grain boundary migration. *Physical review letters* **110**, 265507 (2013).
 - [46] Hamilton, J. C., Siegel, D. J., Daruka, I. & Léonard, F. Why do grain boundaries exhibit finite facet lengths? *Phys. Rev. Lett.* **90**, 246102 (2003).
 - [47] Medlin, D., Cohen, D. & Pond, R. Accommodation of coherency strain by interfacial disconnections at a $90^\circ < 110 >$ grain boundary in gold. *Philosophical magazine letters* **83**, 223–232 (2003).
 - [48] Wu, Z., Zhang, Y. & Srolovitz, D. Grain boundary finite length faceting. *Acta Materialia* **57**, 4278–4287 (2009).
 - [49] Liebscher, C. H. *et al.* Strain-induced asymmetric line segregation at faceted si grain boundaries. *Physical review letters* **121**, 015702 (2018).
 - [50] Meiners, T., Duarte, J., Richter, G., Dehm, G. & Liebscher, C. Tantalum and zirconium induced structural transitions at complex [111] tilt grain boundaries in copper. *Acta Materialia* **190**, 93–104 (2020).
 - [51] Lejček, P. & Hofmann, S. Grain boundary segregation diagrams of α -iron. *Interface Science* **1**, 163–174 (1993).
 - [52] Watanabe, T., Kitamura, S. & Karashima, S. Grain boundary hardening and segregation in alpha iron-tin alloy. *Acta Metallurgica* **28**, 455–463 (1980).
 - [53] Thompson, K. *et al.* In situ site-specific specimen preparation for atom probe tomography. *Ultramicroscopy* **107**, 131–139 (2007).

(a) Sample orientation



(b) Ag free reference

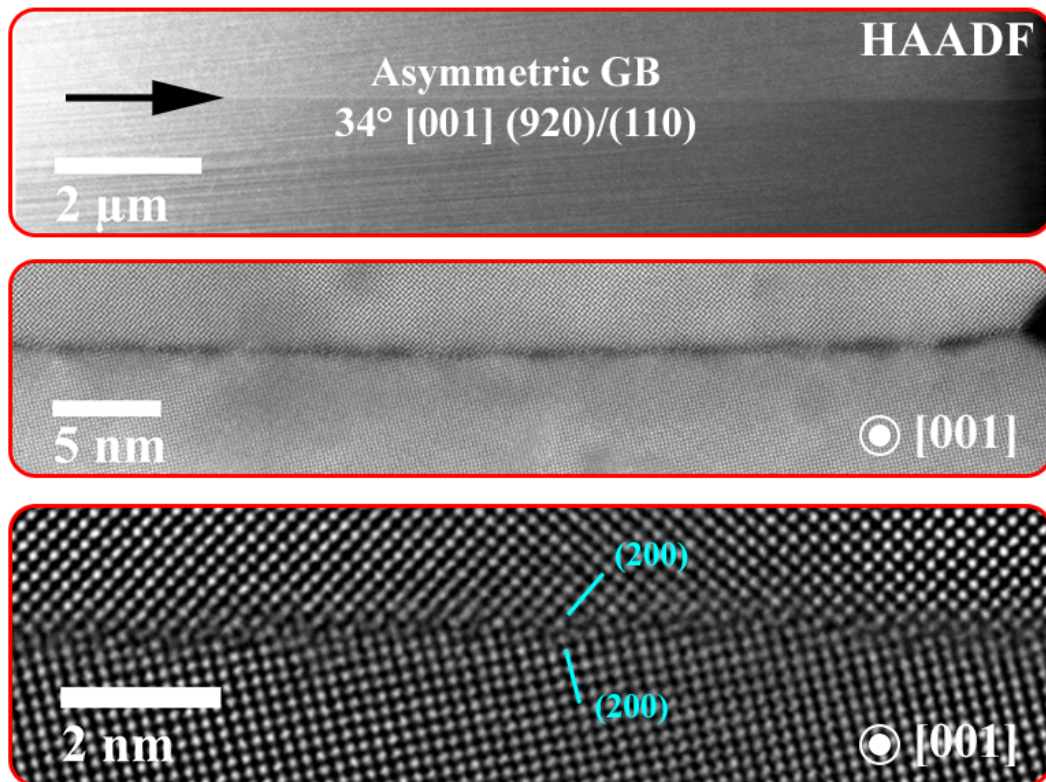


Figure 1: (a) Schematic representation of the diffusion couple's arrangement and the crystallography of the grown bicrystal containing the asymmetric tilt grain boundary and how the boundary behaves after segregation. (b) HAADF-STEM micrographs of the asymmetric, Ag-free, reference boundary at different magnifications. Micrographs are in [001] zone axis orientation.

Ag segregated GB

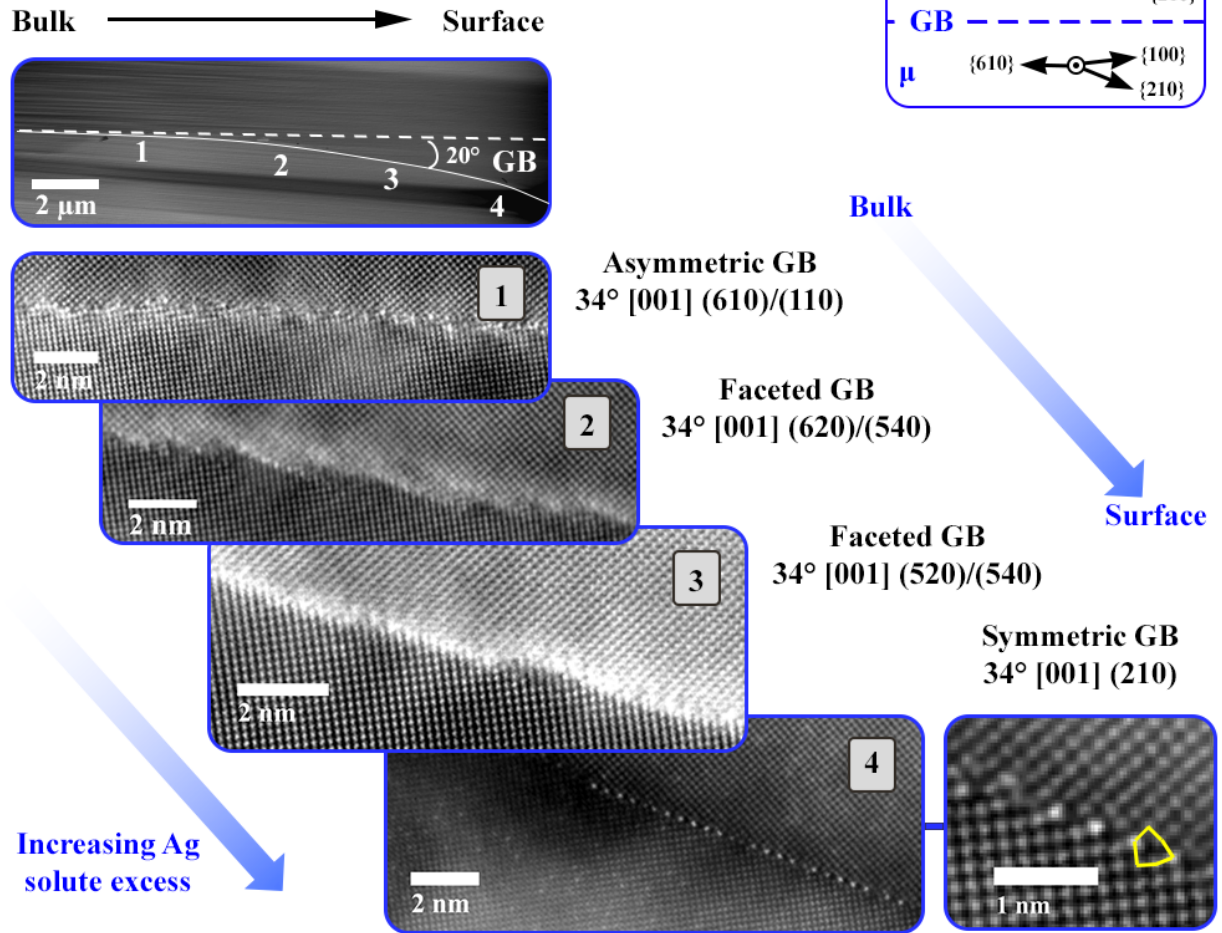


Figure 2: The curved Ag segregated GB as an overview image at lower magnification along with micrographs along a boundary over a distance of about 15 μm indicating the changes from an asymmetric GB (bulk) over the nanofaceted state with increasing symmetric facet segments to a solely symmetric GB (surface) and an atomic resolution micrograph to capture the symmetric (210) GB's kite structure. All HAADF-STEM micrographs were acquired in [001] zone axis orientation.

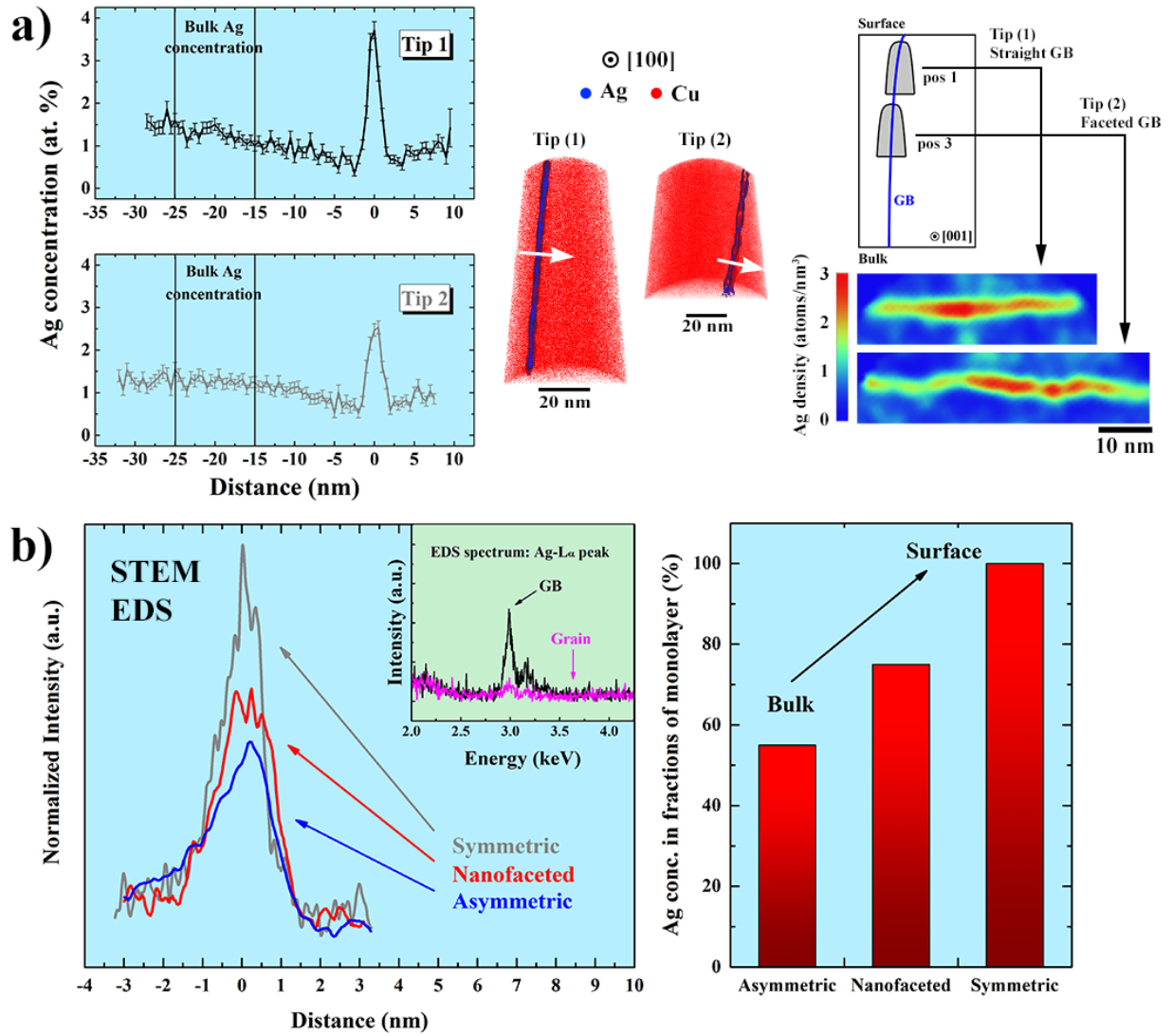


Figure 3: (a) APT results of the Ag segregated GB. The extracted concentration profile across the boundary is given, while Ag density maps are shown representative for two different samples - one at the surface, one deeper into the bulk - highlighting the different GB states. (b) STEM-EDS results across the GB at three representative locations. In the nanofaceted case, EDS information is collected across the GB containing multiple facets. EDS data was collected in zone axis orientation at the exact location where micrographs were recorded.

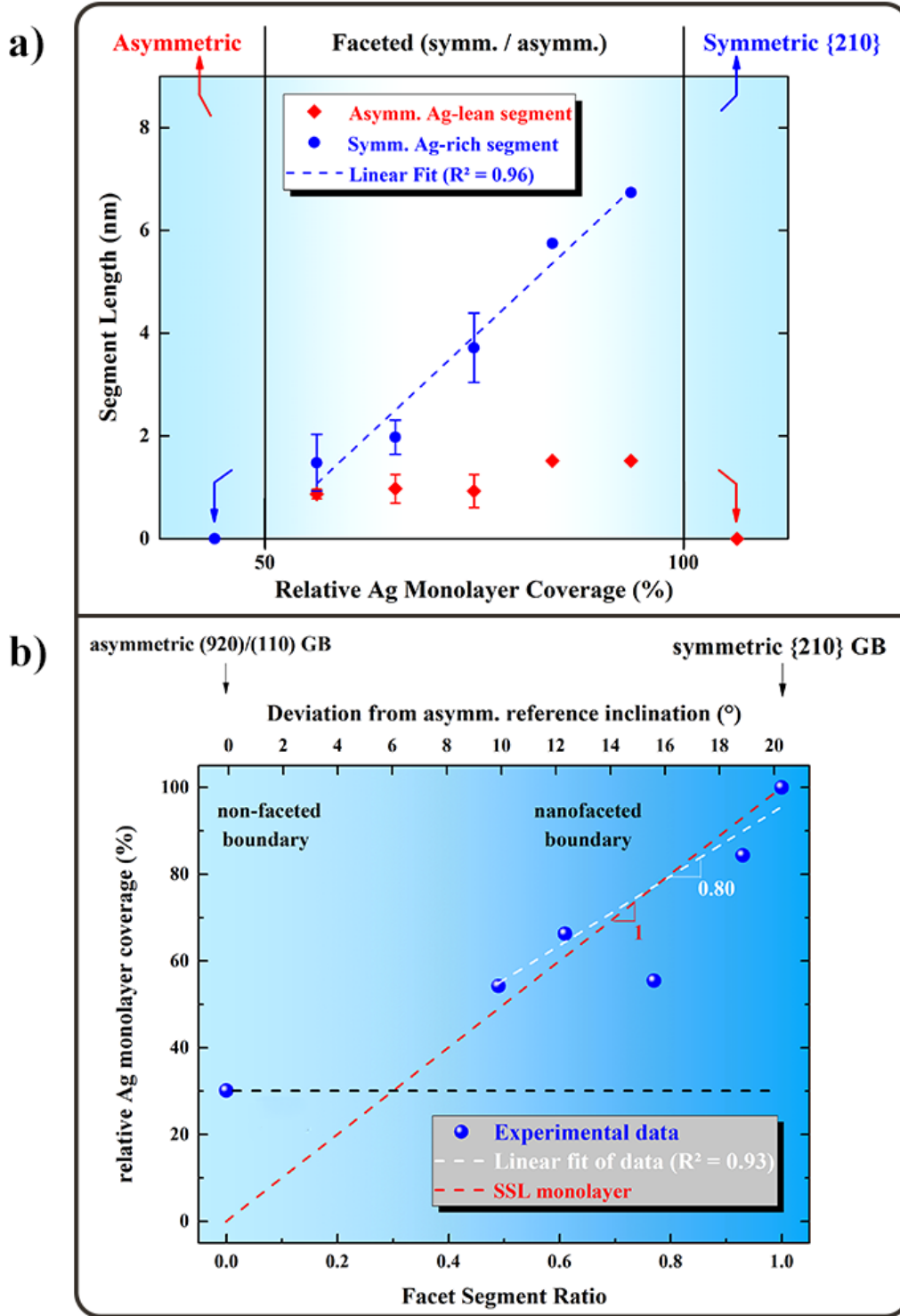


Figure 4: (a) GB faceting diagram presenting the facet segment length evolution along the boundary as a function of Ag solute excess concentration. Three distinct GB states appear: (i) asymmetric and not faceted for low Ag excess, (ii) nanofaceted, preferentially segregated boundary within a solute excess window and (iii) symmetric and not faceted boundary for high Ag excess. (b) Correlation between faceting, inclination and overall inclination of the GB including a linear fit through recorded data points (white line), a straight line to highlight an expected linear dependence of Ag content in facets (red) and the boundary specific Ag excess at the asymmetric GB.